科学通报 2026 年 第 71 卷 第 9 期: 1994 ~ 2002
光电探测材料与器件专题 论 文
《中国科学》杂志社 SCIENCE CHINA PRESS

二维晶格锚定策略合成原子层厚$Mo_{0.92}Er_{0.08}S_2$稀土材料

王肖剑[1†], 张文斌[2†], 白欢[2], 张梦[3], 冯晴亮[1,2*]

1. 西北工业大学化学与化工学院, 西安 710072
2. 积石芯材(西安)科技有限公司, 西安 710061
3. 兰州信息科技学院, 兰州 730300
† 同等贡献
* 联系人, E-mail: fengql@nwpu.edu.cn

2025-09-16 收稿, 2025-12-03 修回, 2025-12-03 接受, 2025-12-04 网络版发表
国家重点研发计划(2021YFA0717600)、国家自然科学基金(52272163)和陕西省杰出青年科学基金(2024JC-JCQN13)资助

摘要 二维稀土(two-dimensional rare-earth, 2D RE)材料由于丰富的4f轨道电子跃迁和多样的发光特性, 在电学、光电等领域受到了广泛的关注. 然而, 实现逻辑运算、成像芯片用的高质量、大面积原子层厚2D RE材料的可控合成仍然是一个重大挑战. 本文中, 我们开发了一种将铒(Er)原子锚定到MoS_2晶格中的二维晶格锚定策略, 合成了高质量、大面积单层$Mo_{0.92}Er_{0.08}S_2$材料, 并研究了其电学与光电特性. 通过飞行时间二次离子质谱(time of flight secondary ion mass spectrometry, TOF-SIMS)和高角度环形暗场扫描透射电子显微镜(high-angle annular dark field scanning transmission electron microscopy, HAADF-STEM)表征, 证实Er原子取代了晶格中的Mo原子位点且均匀地锚定在单层二维晶格中. 通过控制锚定温度和Er前驱体的浓度, 实现了Er原子在MoS_2基质晶格内0.2%~8%锚定率的调控. 与单层纯MoS_2相比, 单层$Mo_{0.92}Er_{0.08}S_2$的载流子迁移率与光响应速度都有了显著提高. 综上所述, 本文提供了一种制备大面积2D RE材料的新方法, 为基于2D RE材料的电子与光电器件的产业化发展创造了有利条件.

关键词 二维稀土材料, 二维晶格锚定, 场效应晶体管, 光电探测器, 快速光响应

稀土(rare-earth, RE)原子具有丰富的激发能级和独特的能级间电子跃迁特性, 能够吸收和发射紫外到红外的光子, 因此RE材料在发光和光探测等领域具有重要的应用前景[1~5]. 二维(2D)稀土材料具有更大的表面能, 并通过维度限域效应显著增强了RE离子独特的光、电性质, 为在原子尺度上精准调控电子自旋和发光行为提供了机遇[6~10]. 目前2D RE材料中, 无论是本征层状RE化合物, 如$RETe_3$(RE = La, Gd)、REOCl(RE = Yb, Eu)、MX_2(M = Eu, Gd; X = Si, Ge)等[11~15], 还是RE-2D异质材料, 如MoS_2/上转换纳米颗粒、石墨烯/RE配合物、钙钛矿/RE等[16~18], 仍无法实现环境稳定型晶圆级2D RE材料可控制备. 理论上, 通过RE原子替代层状2D材料中金属原子, 可控合成大面积、高稳定性2D RE材料的策略是行之有效的[19~22]. 然而, RE离子半径大、熔点高, 且与过渡金属原子的化学价不同, 在晶格中取代过渡金属原子时会引入大的晶格应力, 导致掺杂浓度受限, 难以实现高浓度2D RE材料的可控合成.

单层过渡金属硫族化合物(transition metal dichalcogenides, TMDs)为直接带隙半导体, 兼具强光-物耦合与高载流子迁移率, 可作为宿主晶格精准调控Re的4f能级间电子跃迁[23~25]. Lyu等人[26]在生长衬底上预溅射混合Mo/Er, 以克服Er源高熔点、低蒸气压导致的掺杂瓶颈, 成功实现了Er^{3+}掺杂MoS_2的制备. 结果表明,

引用格式: 王肖剑, 张文斌, 白欢, 等. 二维晶格锚定策略合成原子层厚$Mo_{0.92}Er_{0.08}S_2$稀土材料. 科学通报, 2026, 71: 1994–2002
Wang X, Zhang W, Bai H, et al. Two-dimensional lattice anchoring strategy for the synthesis of atomically thin $Mo_{0.92}Er_{0.08}S_2$ rare-earth materials (in Chinese). Chin Sci Bull, 2026, 71: 1994–2002, doi: 10.1360/CSB-2025-5542

© 2025《中国科学》杂志社

单层Er-MoS_2突破了2D TMDs材料本征带隙的限制, 在980 nm光激发下实现了1530 nm的上转换与800 nm的下转换发光. Xu等人[27]则采用缓释RE前驱体的策略, 将不易挥发的Eu_2O_3原位缓慢转化为易挥发的$EuCl_3$, 实现Eu-MoS_2的制备. 二维晶体场作用下Eu^{3+}发光波长红移至723 nm, 表现出与块体材料截然不同的发光特性. 此外, 脉冲激光沉积技术制备的Yb^{3+}掺杂MoS_2在1002 nm处呈现$^2F_{5/2}\rightarrow{}^2F_{7/2}$跃迁峰, 线宽仅约12 nm, 优于传统块体材料[28]. 综上, 2D RE材料已展示出丰富的发光自由度, 然而受限于低掺杂浓度, 其在电子/光电子器件领域的应用仍待探索.

本文采用晶格锚定的策略, 利用分子筛和NaCl辅助的化学气相沉积(chemical vapor deposition, CVD)法合成了Er掺杂的单层$Mo_{0.92}Er_{0.08}S_2$材料, 并探究了其电子和光电子特性. 通过TOF-SIMS和HAADF-STEM表征, 证实Er原子被均匀地锚定在MoS_2基质晶格中. 通过精准调制锚定温度及Er前驱体分压, 利用热力学-动力学协同控制, 实现了MoS_2基质晶格中0.2%~8%Er原子锚定比例的调控. 电输运与光响应测试结果表明, 单层$Mo_{0.92}Er_{0.08}S_2$保持n型导电特性, 且载流子迁移率和光响应上升/下降时间较本征单层MoS_2显著提升. 该工作为RE掺杂2D材料在电子、光电子领域的应用开辟了一条新途径.

1 实验方法

(i) 单层$Mo_xEr_{1-x}S_2$的制备: 以MoO_3(10 mg)和Er_2O_3(30 mg)粉末分别作为Mo源和Er源的前驱体. 将Er前驱体粉末与NaCl(1 mg)均匀混合, 置于管式炉中心温区的石英舟中. 在混合粉末上覆盖一层分子筛, 并将清洗干净的SiO_2/Si衬底倒扣至前驱体上方. 将S粉(80 mg)作为S源置于温度为200 ℃的管式炉上游温区处. 以300 sccm的流速通10 min氩气后, 管式炉以30 ℃/min的速率升温至700~900 ℃, 并在700~900 ℃保温10 min, 随后自然冷却至室温.

(ii) 结构和组分表征: 光学显微镜(optical microscopy, OM)图像采用Olympus BX51显微镜进行表征; 原子力显微镜(atomic force microscopy, AFM)表征采用Bruker Dimension ICON进行; TOF-SIMS测量采用PHI nanoTOF II飞行时间模拟仪, 样品在高分辨率模式下以能量为30 keV的Bi_3^+激发测试; X射线光电子能谱(X-ray photoelectron spectroscopy, XPS)采用AXIS Ultra DLD进行测试; 拉曼与光致发光(photoluminescence, PL)光谱使用WITec Alpha300R利用532 nm激光器进行测试; HAADF-STEM图像使用TEMs(JEOL JEM2100-CF和Thermoscientific Themis Z)进行表征.

(iii) 单层$Mo_{0.92}Er_{0.08}S_2$器件的制备与测试: 将单层$Mo_{0.92}Er_{0.08}S_2$转移到新的SiO_2/Si衬底上, 并将物理掩模版放置在材料表面. 使用热蒸发镀膜技术, 先后蒸镀5与50 nm的Cr/Au电极, 最后去除掩模版, 得到单层$Mo_{0.92}Er_{0.08}S_2$器件. 利用CGO-8探针台、2614B源表与MDL-III 532 nm激光器构成测试系统, 进行电学与光电性能测试.

2 结果与讨论

基于晶格锚定策略, 采用分子筛和NaCl辅助的CVD法在SiO_2/Si衬底上制备了单层$Mo_{0.92}Er_{0.08}S_2$材料(图S1). 研究表明, NaCl可促进Er前驱体挥发并降低反应势垒[27]; 分子筛的纳米孔道可确保前驱体的缓慢均匀释放[29]; 且900 ℃的高生长温度可克服高浓度掺杂带来的晶格应力, 促进单层$Mo_{0.92}Er_{0.08}S_2$材料在SiO_2/Si衬底上的大面积制备(生长的详细过程见实验部分). 图1(a)分别展示了纯MoS_2和$Mo_{0.92}Er_{0.08}S_2$的原子结构示意图, 其均属于六方晶系(空间群: $P6_3/mmc$)结构, 其中Er原子取代Mo原子位点被锚定在MoS_2晶格中. $Mo_{0.92}Er_{0.08}S_2$的OM图像显示其形貌呈现类圆形, 如图1(b)所示. AFM图像显示$Mo_{0.92}Er_{0.08}S_2$的厚度约为0.71 nm(图1(c)), 与单层纯MoS_2相似, 证明MoS_2晶格在锚定Er原子后并没有发生明显的结构破坏与转变. 为了证明Er原子被均匀锚定在MoS_2晶格中, 使用TOF-SIMS对单层$Mo_{0.92}Er_{0.08}S_2$进行了元素面扫表征. 图S2(a~d)和图S2(e~h)分别为$Mo_{0.92}Er_{0.08}S_2$材料中所含元素在正离子模式和负离子模式下的TOF-SIMS图. 正离子模式下, 在材料中检测到显著的Er信号, 表明Er被成功地掺杂到基质MoS_2中. 此外, 图1(d~g)分别展示了Mo、Er、S和其三个元素叠加的TOF-SIMS改色面扫图. 不同元素的分布在空间上是一致的, 且Er具有均匀的颜色衬度, 表明Er被均匀锚定在MoS_2材料中.

进一步地, 单层$Mo_{0.92}Er_{0.08}S_2$的XPS全光谱证实了Mo、Er、S三元素共存(图S3(a)). 高分辨XPS(图1(h))显示, 本征MoS_2的Mo $3d_{5/2}$和Mo $3d_{3/2}$分别位于229.78与232.94 eV; 锚定Er后, $Mo_{0.92}Er_{0.08}S_2$材料中对应峰移至228.88与232.01 eV. 此外, S 2p能级峰亦同步向低结合能移动(图S3(b)). 这是由于Er掺杂导致Mo与S原子周围化学环境改变. 同时, 175.2 eV处出现清晰Er 4d能级

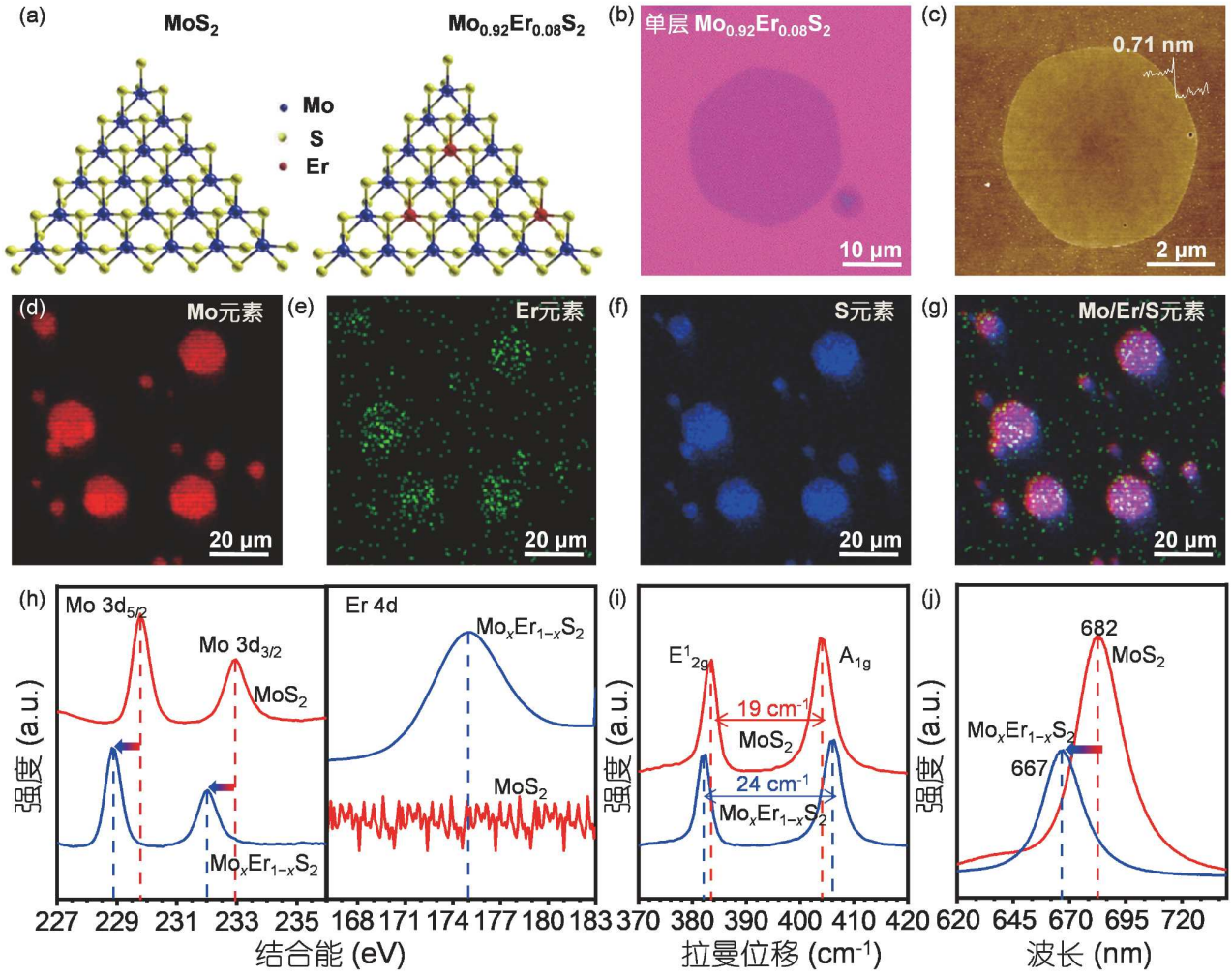


图 1 单层$Mo_{0.92}Er_{0.08}S_2$的组分与结构. (a) MoS_2和$Mo_{0.92}Er_{0.08}S_2$的原子结构示意图. (b, c) 单层$Mo_{0.92}Er_{0.08}S_2$在SiO_2/Si衬底上的OM和AFM图像. (d~g) Mo、Er、S和三个元素叠加的TOF-SIMS改色面扫图. (h) 单层MoS_2和$Mo_{0.92}Er_{0.08}S_2$的Mo 3d和Er 4d的XPS精细谱. (i, j) 单层MoS_2和$Mo_{0.92}Er_{0.08}S_2$的拉曼和PL光谱

Figure 1 Composition and structure of monolayer $Mo_{0.92}Er_{0.08}S_2$. (a) Atomic diagrams of MoS_2 and $Mo_{0.92}Er_{0.08}S_2$. (b, c) OM and AFM images of monolayer $Mo_{0.92}Er_{0.08}S_2$ on SiO_2/Si substrate. (d–g) Rendered TOF-SIMS mapping images of Mo, Er, S and three superimposed elements. (h) High-resolution XPS spectra of Mo 3d and Er 4d of monolayer MoS_2 and $Mo_{0.92}Er_{0.08}S_2$. (i, j) Raman and PL spectra of monolayer MoS_2 and $Mo_{0.92}Er_{0.08}S_2$

峰, 确认Er被锚定在晶格中. 此外, 如图1(i)所示, 单层$Mo_{0.92}Er_{0.08}S_2$的拉曼振动模相较纯MoS_2也发生了明显变化. 单层MoS_2的E^1_{2g}和A_{1g}峰分别位于383和403 cm^{-1}, 而单层$Mo_{0.92}Er_{0.08}S_2$的E^1_{2g}和A_{1g}峰分别位于382和406 cm^{-1}. 与MoS_2相比, 单层$Mo_{0.92}Er_{0.08}S_2$的E^1_{2g}和A_{1g}峰间距变为24 cm^{-1}(纯MoS_2为20 cm^{-1})[30], $Mo_{0.92}Er_{0.08}S_2$中的E^1_{2g}峰有轻微的红移, A_{1g}峰有明显的蓝移, 这是由于Er-S键的形成导致了晶胞面外振动的改变. 此外, 单层$Mo_{0.92}Er_{0.08}S_2$的拉曼映射显示E^1_{2g}和A_{1g}峰强度均匀, 样品具有大面积均匀性和高结晶质量(图S4). 图1(j)为单层$Mo_{0.92}Er_{0.08}S_2$和MoS_2的PL光谱. $Mo_{0.92}Er_{0.08}S_2$的PL峰位于667 nm, 与MoS_2(682 nm)相比蓝移了15 nm, 这可能是掺杂引入的杂质能级与本征MoS_2能级杂化的结果[1].

进一步利用球差校正透射电子显微镜对单层$Mo_{0.92}Er_{0.08}S_2$的原子结构进行解析. 图2(a)显示了单层$Mo_{0.92}Er_{0.08}S_2$转移到透射载网上的低倍率图像, 并在此区域进行选择区域电子衍射(SAED)标定. 图2(b)展示出一套六方对称的衍射斑点, 其中(100)晶面间距为0.26 nm, (110)晶面间距为0.16 nm. 众所周知, HAADF-STEM图像(图2(c))中, 原子的亮度与原子序数(Z)成正比, 可清晰区分S(Z = 16)、Mo(Z = 42)与Er(Z = 68)原

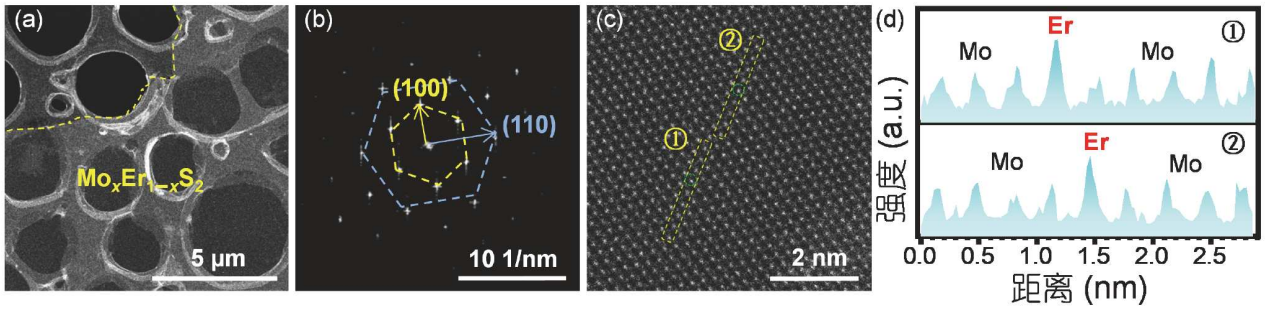


图 2 单层$Mo_{0.92}Er_{0.08}S_2$的原子结构. (a) 单层$Mo_{0.92}Er_{0.08}S_2$低放大倍数透射图像. (b) 单层$Mo_{0.92}Er_{0.08}S_2$的电子衍射花样图像. (c) 单层$Mo_{0.92}Er_{0.08}S_2$原子分辨率的HAADF-STEM图像. (d) 图(c)黄框区域中的原子强度抛线图

Figure 2 Atomic structure of monolayer $Mo_{0.92}Er_{0.08}S_2$. (a) Low-magnification TEM image of monolayer $Mo_{0.92}Er_{0.08}S_2$. (b) The SAED pattern of monolayer $Mo_{0.92}Er_{0.08}S_2$. (c) Atomic-resolution HAADF-STEM image of monolayer $Mo_{0.92}Er_{0.08}S_2$. (d) Corresponding intensity line profiles along with yellow boxes in (c)

子. 绿色圆框标记位点亮度显著高于邻近Mo原子, 对应Er取代Mo的替位构型. 从图2(d)所示黄框区域的原子强度抛线图可直观地看出, Er原子锚定在Mo原子位点, 且具有更强的原子亮度. 此外, 更多不同样品区域的HAADF-STEM图像表明, Er被随机、均匀锚定在MoS_2晶格中(图S5).

为了揭示MoS_2晶格锚定Er的作用规律, 通过调节锚定温度与Er前驱体浓度进行了研究. 图3(a)分别展示了750、800、850和900℃温度下制备单层$Mo_xEr_{1-x}S_2$的OM与AFM图像. 随着锚定温度的增加, 样品的形貌从规则三角形往不规则圆形转变. 这可能是随着晶格中Er含量的增加, 破坏了纯MoS_2晶格三重对称性导致的. 在不同温度制备的单层$Mo_xEr_{1-x}S_2$的XPS光谱进一步表明, 样品中Er的含量随着合成温度的升高而增加, 如图3(b)所示. 根据单层$Mo_xEr_{1-x}S_2$中Er元素与Mo元素的峰面积比值计算, 合成温度为750、800、850和900℃时, Er锚定比例分别为0.2%、1%、5%和8%. 此外, 不同温度制备的单层$Mo_xEr_{1-x}S_2$的Mo 3d和S 2p能级的XPS光谱显示, 随着合成温度的升高, 其XPS峰向低结合能方向移动(图S6(a, b)). 图3(c)中Mo $3d_{3/2}$、Mo $3d_{5/2}$、S $2p_{1/2}$和S $2p_{3/2}$能级的结合能随合成温度变化曲线直观地展示了此规律. 为了解析不同温度制备的单层$Mo_xEr_{1-x}S_2$的组分和电子结构之间的关系, 对样品进行了拉曼和PL分析. 不同温度制备单层$Mo_xEr_{1-x}S_2$的拉曼光谱显示, 随着Er比例的增加, E^1_{2g}峰出现红移, A_{1g}峰出现蓝移(图3(d)). 图3(f)为E^1_{2g}和A_{1g}峰波数随合成温度变化的曲线图, 可以看出随着Er比例的增加, E^1_{2g}和A_{1g}两种振动模式的波数差值越来越大. 不同温度制备的单层$Mo_xEr_{1-x}S_2$的PL光谱显示, 随着Er浓度的增加, PL峰出现蓝移(图3(e)). PL发射波长随锚定温度变化的曲线进一步显示, 随着Er浓度的增加, 其峰位从681 nm蓝移到666 nm, 如图3(g)所示. 这些变化规律与上文展示的单层纯MoS_2与$Mo_{0.92}Er_{0.08}S_2$的变化规律一致. 高温提供的能量可以克服Er锚定过程中在MoS_2晶格产生的高晶格应力, 从而提高Er的锚定比例. 此外, 对于分子筛孔隙率、H_2流速的调控研究细节见图S7~S9. 结果表明, 40%孔隙率的分子筛通过延缓前驱体在衬底表面的吸附与扩散, 有效调控成核与生长过程, 而H_2对$Mo_{0.92}Er_{0.08}S_2$生长无显著影响.

采用物理掩膜技术, 在SiO_2/Si衬底表面的单层$Mo_{0.92}Er_{0.08}S_2$材料上热蒸发Cr/Au(5/50 nm)电极, 构筑背栅场效应晶体管. 图4(a)展示了单层$Mo_{0.92}Er_{0.08}S_2$器件在SiO_2/Si衬底上的OM图像. 图4(b)与S10(a)分别展示了单层$Mo_{0.92}Er_{0.08}S_2$和纯MoS_2的输出特性曲线. 相比于纯MoS_2器件, 单层$Mo_{0.92}Er_{0.08}S_2$器件的输出曲线表现出更好的线性度, 证明单层$Mo_{0.92}Er_{0.08}S_2$与电极间具有低的接触电阻. 并且, 在相同的偏压与栅压下, 单层$Mo_{0.92}Er_{0.08}S_2$器件的导通电流也大于MoS_2. 单层$Mo_{0.92}Er_{0.08}S_2$和纯MoS_2器件的转移特性曲线如图4(c)与S10(b)所示, 其均表现为n型半导体导电特性. 根据迁移率计算公式:

$$\mu = \frac{L}{W} \times \frac{1}{C_g \times V_{ds}} \times \frac{dI_{ds}}{dV_{ds}}, \quad (1)$$

其中, L、W、C_g、V_{ds}、I_{ds}和V_{gs}分别表示沟道长度、沟道宽度、单位面积栅极电容、偏压、漏源电流和栅压, 计算得到单层$Mo_{0.92}Er_{0.08}S_2$的迁移率为36.5 $cm^2\ V^{-1}\ s^{-1}$, 是同等器件加工和测试条件下纯MoS_2(0.41 $cm^2\ V^{-1}\ s^{-1}$)的89倍. 与文献报道的纯MoS_2基器件相比, 其也表

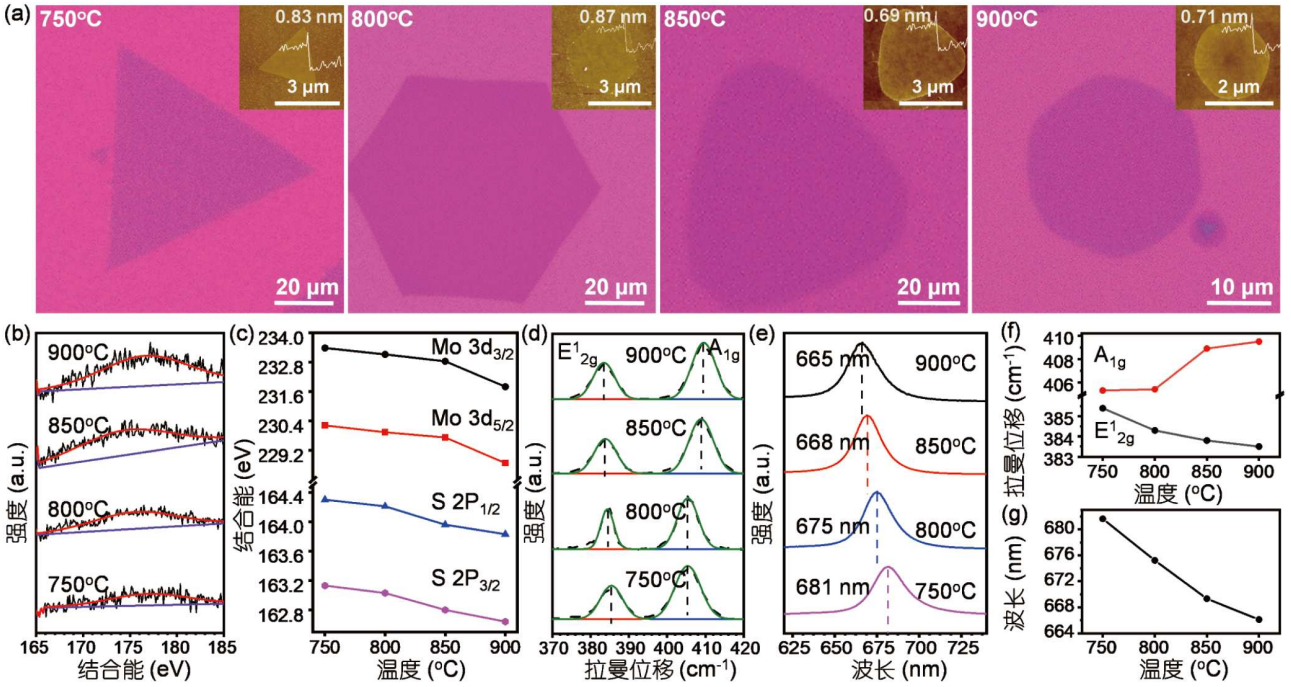


图 3 不同温度合成单层$Mo_xEr_{1-x}S_2$的结构与组分. (a) 在750、800、850和900℃下合成单层$Mo_xEr_{1-x}S_2$的OM和AFM图像. (b) 不同温度制备单层$Mo_xEr_{1-x}S_2$的Er 4d能级的XPS光谱. (c) Mo $3d_{3/2}$、Mo $3d_{5/2}$、S $2p_{1/2}$和S $2p_{3/2}$能级的结合能随锚定温度的变化曲线图. (d, e) 不同温度下合成单层$Mo_xEr_{1-x}S_2$的拉曼光谱和PL光谱. (f) E^1_{2g}和A_{1g}峰的拉曼波数随锚定温度的位移曲线. (g) PL发射波长随锚定温度的变化曲线

Figure 3 Composition and structure of $Mo_xEr_{1-x}S_2$ synthesized at different temperatures. (a) OM and AFM images of $Mo_xEr_{1-x}S_2$ synthesized at 750, 800, 850 and 900℃, respectively. (b) XPS spectra of Er 4d of $Mo_xEr_{1-x}S_2$ synthesized at different temperatures. (c) Plots of binding energy of Mo $3d_{3/2}$, Mo $3d_{5/2}$, S $2p_{1/2}$ and S $2p_{3/2}$ as a function of growth temperature. (d, e) Raman and PL spectra of $Mo_xEr_{1-x}S_2$ synthesized at different temperatures, respectively. (f) Plots of Raman shift of E^1_{2g} and A_{1g} peaks as a function of growth temperature. (g) Plots of fluorescence emission wavelength as a function of growth temperature

现出有竞争力的迁移率(表S2).

进一步研究了基于单层$Mo_{0.92}Er_{0.08}S_2$的光电探测性能. 如图4(d)展示了532 nm脉冲激光辐照下, 重复且稳定的光响应I-t图像. 在2 V的工作偏压下, 光辐照会导致器件电流增大, 这与纯MoS_2的光电导效应相同. 此外, 单层$Mo_{0.92}Er_{0.08}S_2$的光响应时间与纯MoS_2相比得到了巨大的提高. 如图4(e)所示, 单层$Mo_{0.92}Er_{0.08}S_2$的光响应上升时间和衰减时间分别为49与50 ms, 而纯MoS_2的光响应上升时间和衰减时间分别为106与204 ms(上升和衰减时间分别为光电流从10%上升到90%和光电流从90%衰减到10%所花费的时间). 为了进一步评估器件性能, 单层$Mo_{0.92}Er_{0.08}S_2$器件在功率密度为7.1~12.73 mW/cm^{2}的532 nm激光照射下的光响应曲线如图S11所示. 随着激光功率的降低, 光电流也随之降低. 光响应度(photoresponsivity, R)作为评估材料产生光电流能力的参数, 其计算公式为

$$R = \frac{I_{ph}}{P}, \tag{2}$$

其中, I_{ph}为光电流, P为照射在沟道面积上的光功率密度. 图4(f)展示了激光功率密度与I_{ph}及R的依赖关系图: 随着激光功率的降低, I_{ph}随之降低, 而R持续增大. 测得最大I_{ph}与R分别为142 nA与204 mA/W, 较之纯MoS_2在12.73 mW/cm^{2}功率密度的激光照射下的R提高约20倍. 具有丰富4f能级的Er离子可作为光吸收剂, 高效吸收光子能量[18], 且光载流子可以非辐射跃迁的方式传递给基质材料[6]. 这可能是单层$Mo_{0.92}Er_{0.08}S_2$材料具有优异的光电性能的原因. 综上, Er原子锚定在单层MoS_2晶格中, 可提高材料的载流子迁移率与光响应时间, 为构建高性能电子与光电子器件提供有效途径.

3 结论

综上所述, 本工作开发了一种晶格锚定策略, 通过把稀土Er原子锚定在2D MoS_2晶格中, 实现了单层$Mo_{0.92}Er_{0.08}S_2$材料的可控制备, 通过优化锚定温度与前驱体浓度实现了Er原子0.2%~8%锚定比例的调控. 利用TOF-SIMS与HAADF-STEM证实了Er原子被均匀锚定在

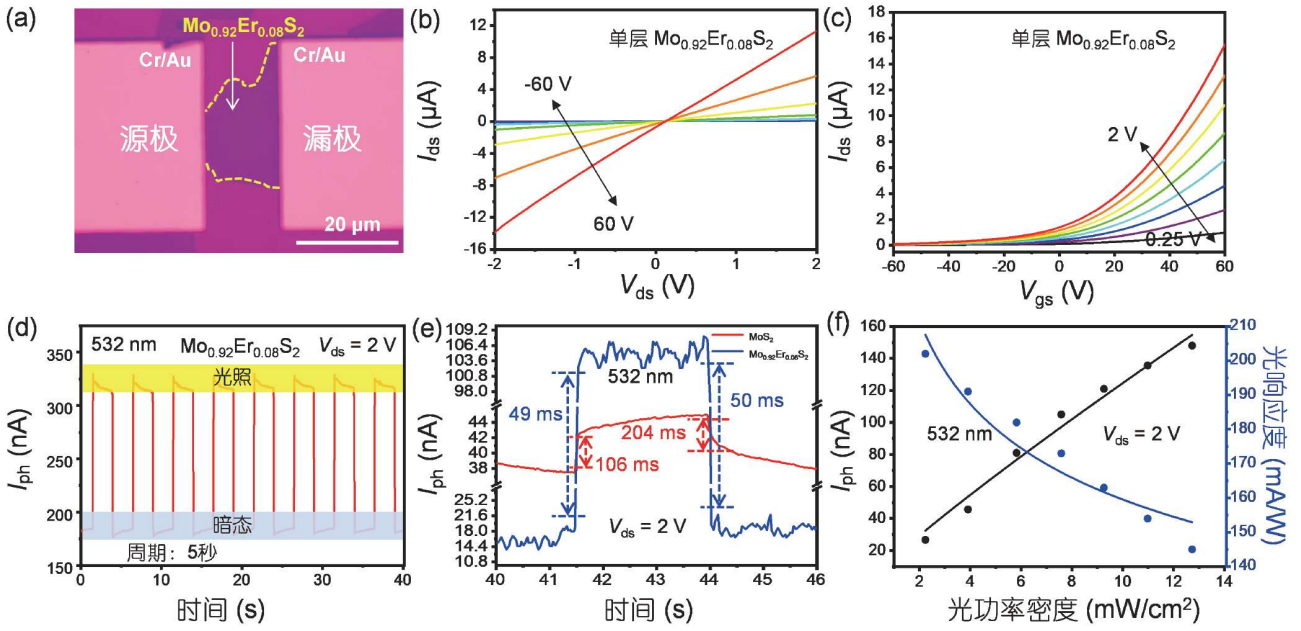


图 4 基于单层$Mo_{0.92}Er_{0.08}S_2$的电学输运与光电响应. (a) 基于单层$Mo_{0.92}Er_{0.08}S_2$的器件的OM图像. (b, c) 分别为单层$Mo_{0.92}Er_{0.08}S_2$场效应晶体管的输出特性曲线与转移特性曲线. (d) 单层$Mo_{0.92}Er_{0.08}S_2$光电探测器在532 nm激光辐照下的光响应*I*-*t*图. (e) 单层$Mo_{0.92}Er_{0.08}S_2$与纯MoS_2光电探测器的光响应时间对比图. (f) 单层$Mo_{0.92}Er_{0.08}S_2$光电探测器光功率依赖的光电流与响应度关系曲线

Figure 4 Electrical transport and photoresponse of monolayer $Mo_{0.92}Er_{0.08}S_2$ and MoS_2 devices. (a) OM image of device structure for monolayer $Mo_{0.92}Er_{0.08}S_2$. (b, c) Typical output and transfer characteristic curves of monolayer $Mo_{0.92}Er_{0.08}S_2$ FETs, respectively. (d) Photocurrent as a function of time of monolayer $Mo_{0.92}Er_{0.08}S_2$ device under light illumination with 532 nm. (e) Comparative plot of the photoresponse rate between monolayer $Mo_{0.92}Er_{0.08}S_2$ and pure MoS_2 photodetectors. (f) Plots of photocurrent and responsivity as a function of power density in monolayer $Mo_{0.92}Er_{0.08}S_2$ photodetectors

MoS_2晶格中. 相比于纯MoS_2器件, 单层$Mo_{0.92}Er_{0.08}S_2$器件具有更高的载流子迁移率(36.5 cm^2 V^{-1} s^{-1})与更快的光响应时间(50 ms). 我们的工作为适用于电子与光电子器件2D RE材料的制备开辟了一条新的途径.

参考文献

1 Wen S, Zhou J, Zheng K, et al. Advances in highly doped upconversion nanoparticles. Nat Commun, 2018, 9: 2415

2 Wu S, Min H, Shi W, et al. Multicenter metal–organic framework-based ratiometric fluorescent sensors. Adv Mater, 2020, 32: 1805871

3 Liu B, Chen Y, Li C, et al. Poly(acrylic acid) modification of Nd^{3+}-sensitized upconversion nanophosphors for highly efficient UCL imaging and pH-responsive drug delivery. Adv Funct Mater, 2015, 25: 4717–4729

4 Liu Y, Tu D, Zhu H, et al. A strategy to achieve efficient dual-mode luminescence of Eu^{3+} in lanthanides doped multifunctional $NaGdF_4$ nanocrystals. Adv Mater, 2010, 22: 3266–3271

5 Pan Y, Xie X, Huang Q, et al. Inherently Eu^{2+}/Eu^{3+} codoped Sc_2O_3 nanoparticles as high-performance nanothermometers. Adv Mater, 2018, 30: 1705256

6 Chen P, Han W, Zhao M, et al. Recent advances in 2D rare earth materials. Adv Funct Mater, 2021, 31: 2008790

7 Zhang Z, Zhao H, Zhang C, et al. Rare-earth-incorporated low-dimensional chalcogenides: dry-method syntheses and applications. InfoMat, 2020, 2: 466–482

8 Huang P, Wu Y, Gao M, et al. Scalable synthesis of 2D ErOCl with sub-meV narrow emissions at telecom band. Adv Mater, 2025, 37: 2404698

9 Chen P, Xu X, Li D, et al. 2D van der Waals rare earth material based ratiometric luminescence thermography integrated on micro–nano devices vertically. Adv Opt Mater, 2022, 10: 2102102

10 Chen P, Li D, Li Z, et al. Electric-tunable photoluminescence of 2D ErOCl for high-security encryption of programmable information. Adv Opt Mater, 2022, 10: 2102562

11 Ru N, Fisher I R. Thermodynamic and transport properties of YTe_3, $LaTe_3$, and $CeTe_3$. Phys Rev B, 2006, 73: 033101

12 Zhao L L, Mehlman M S, Besara T, et al. Thermodynamic and transport properties of RSn_2 (R=Tb–Tm, Lu, Y) single crystals. J Magn Magn Mater, 2013, 341: 6–16
13 Yao Y, Zhang Y, Xiong W, et al. Growth and Raman scattering investigation of a new 2D MOX material: YbOCl. Adv Funct Mater, 2019, 29: 1903017
14 Tokmachev A M, Averyanov D V, Parfenov O E, et al. Emerging two-dimensional ferromagnetism in silicene materials. Nat Commun, 2018, 9: 1672
15 Tokmachev A M, Averyanov D V, Taldenkov A N, et al. Lanthanide f^7 metalloxenes – a class of intrinsic 2D ferromagnets. Mater Horiz, 2019, 6: 1488–1496
16 Sokolov I S, Averyanov D V, Parfenov O E, et al. 2D ferromagnetism in europium/graphene bilayers. Mater Horiz, 2020, 7: 1372–1378
17 Ghosh S, Chiang W C, Fakhri M Y, et al. Ultrasensitive broadband photodetector using electrostatically conjugated MoS_2-upconversion nanoparticle nanocomposite. Nano Energy, 2020, 67: 104258
18 Zhang X, Yang S, Zhou H, et al. Perovskite–erbium silicate nanosheet hybrid waveguide photodetectors at the near-infrared telecommunication band. Adv Mater, 2017, 29: 1604431
19 Bai G, Yuan S, Zhao Y, et al. 2D layered materials of rare-earth Er-doped MoS_2 with NIR-to-NIR down- and up-conversion photoluminescence. Adv Mater, 2016, 28: 7472–7477
20 Du Z, Yang S, Li S, et al. Conversion of non-van der Waals solids to 2D transition-metal chalcogenides. Nature, 2020, 577: 492–496
21 Yang Y, Pu H, Di J, et al. Synthesis and characterization of monolayer Er-doped MoS_2 films by chemical vapor deposition. Scripta Mater, 2018, 152: 64–68
22 Lun M, Wu W, Xing Z, et al. Upconversion photoluminescence of Er^{3+} and Yb^{3+} codoped MoS_2 powders. J Lumin, 2020, 223: 117189
23 Maiti R, Patil C, Saadi M A S R, et al. Strain-engineered high-responsivity $MoTe_2$ photodetector for silicon photonic integrated circuits. Nat Photonics, 2020, 14: 578–584
24 Chowdhury T, Kim J, Sadler E C, et al. Substrate-directed synthesis of MoS_2 nanocrystals with tunable dimensionality and optical properties. Nat Nanotechnol, 2020, 15: 29–34
25 Liao M, Wei Z, Du L, et al. Precise control of the interlayer twist angle in large scale MoS_2 homostructures. Nat Commun, 2020, 11: 2153
26 Lyu Y, Wu Z, Io W F, et al. Observation and theoretical analysis of near-infrared luminescence from CVD grown lanthanide Er doped monolayer MoS_2 triangles. Appl Phys Lett, 2019, 115: 153105
27 Xu D, Chen W, Zeng M, et al. Crystal-field tuning of photoluminescence in two-dimensional materials with embedded lanthanide ions. Angew Chem Int Ed, 2018, 57: 755–759
28 Maddi C, Aswin J R, Scott A, et al. Structural, spectroscopic, and excitonic dynamic characterization in atomically thin Yb^{3+}-doped MoS_2, fabricated by femtosecond pulsed laser deposition. Adv Opt Mater, 2019, 7: 1900753
29 Wang X, Shang J, Zhu M, et al. Controlled growth of large-scale uniform 1T′ $MoTe_2$ crystals with tunable thickness and their photodetector applications. Nanoscale Horiz, 2020, 5: 954–959
30 Li T, Guo W, Ma L, et al. Epitaxial growth of wafer-scale molybdenum disulfide semiconductor single crystals on sapphire. Nat Nanotechnol, 2021, 16: 1201–1207

补充材料

图S1 CVD生长法在SiO_2/Si衬底上合成高掺杂浓度的2D RE掺杂单层$Mo_xEr_{1-x}S_2$示意图
图S2 $Mo_{0.92}Er_{0.08}S_2$在正负离子模式下的TOF-SIMS图
图S3 单层$Mo_{0.92}Er_{0.08}S_2$的XPS谱图
图S4 SiO_2/Si衬底上单层$Mo_{0.92}Er_{0.08}S_2$拉曼光谱的峰值强度映射
图S5 单层$Mo_{0.92}Er_{0.08}S_2$中随机选取不同区域的HAADF-STEM图像.
图S6 不同温度(750、800、850、900℃)下合成的$Mo_xEr_{1-x}S_2$的Mo 3d和S 2p高分辨率XPS光谱
图S7 使用不同孔隙率分子筛制备$Mo_{0.92}Er_{0.08}S_2$的OM图像
图S8 退火前后的分子筛结构及其孔隙率分析
图S9 H_2流速对$Mo_{0.92}Er_{0.08}S_2$生长的影响
图S10 单层MoS_2 FET的输出与转移特性曲线
图S11 在532 nm激光不同功率密度照射下单层$Mo_{0.92}Er_{0.08}S_2$的光响应
表S1 不同文献报道的稀土掺杂MoS_2材料
表S2 不同文献报道的MoS_2基FET迁移率

本文以上补充材料见网络版csb.scichina.com. 补充材料为作者提供的原始数据, 作者对其学术质量和内容负责.

Summary for “二维晶格锚定策略合成原子层厚$Mo_{0.92}Er_{0.08}S_2$稀土材料”

Two-dimensional lattice anchoring strategy for the synthesis of atomically thin $Mo_{0.92}Er_{0.08}S_2$ rare-earth materials

Xiaojian Wang[1†], Wenbin Zhang[2†], Huan Bai[2], Meng Zhang[3] & Qingliang Feng[1,2*]

[1] *School of Chemistry and Chemical Engineering, Northwestern Polytechnical University, Xi'an 710072, China*
[2] *Jishi Chip & Materials (Xi'an) Technology Corp. Ltd, Xi'an 710061, China*
[3] *Lanzhou University of Information Science and Technology, Lanzhou 730300, China*
† Equally contributed to this work
* Corresponding author, E-mail: fengql@nwpu.edu.cn

Two-dimensional rare-earth (2D RE) materials have attracted significant research interest in fields such as electronics and optoelectronics, owing to their abundant 4f electron transitions and diverse luminescent properties. Currently, the preparation of RE-doped MoS_2 has been achieved through strategies such as pre-deposition of RE precursors, controlled release of RE precursors, and pulsed laser deposition. Furthermore, the properties of these two-dimensional systems, such as upconversion luminescence resulting from the modulated 4f energy levels, were thoroughly investigated. Nevertheless, the synthesis of large-area and atomically thick 2D RE materials, which are essential for logic operations and imaging chips, remains a significant challenge. Herein, we report a 2D lattice anchoring strategy, which enables the anchoring of erbium (Er) atoms into the MoS_2 lattice for the synthesis of high-quality, large-area monolayer $Mo_{0.92}Er_{0.08}S_2$, thereby facilitating the investigation of its electrical and photoelectronic properties. Time-of-flight secondary ion mass spectrometry (TOF-SIMS) and high-angle annular dark-field scanning transmission electron microscopy (HAADF-STEM) confirmed that Er atoms are uniformly anchored into the MoS_2 host lattice by directly substituting for Mo atoms. The Er doping concentration in the material was determined employing X-ray Photoelectron Spectroscopy (XPS) and STEM. By controlling the anchoring temperature and the concentration of the erbium precursor, the Er anchoring ratio within the lattice was tuned from 0.2% to 8%. A high growth temperature enables the overcoming of lattice strain induced by RE doping and facilitates an increase in the doping concentration. In addition, NaCl acts as a catalyst to lower the melting point of the rare-earth precursor and facilitates the lateral epitaxial growth of $Mo_{0.92}Er_{0.08}S_2$. And, the structurally stable porous molecular sieve at high temperatures provides favorable channels for the controlled release of the RE precursor. The synergistic strategy employing high growth temperature, NaCl and molecular sieves is therefore pivotal in realizing high-concentration Er doping within monolayer MoS_2. Interestingly, as the Er doping concentration increases, the sample morphology evolves from regular triangles to irregular circular shapes. This is likely attributed to the disruption of the pristine MoS_2's threefold symmetry by the high-concentration Er doping. Compared to pristine MoS_2 monolayer, the monolayer $Mo_{0.92}Er_{0.08}S_2$ device exhibited a significantly enhanced carrier mobility and photoresponse rate. This effect originates from the rich 4f electronic states of rare-earth dopants, functioning as highly effective light absorbers. Consistent with previous studies on RE hybrid materials, this effect enhances the photoconversion efficiency of the intrinsic MoS_2, imparting superior photocurrent and response speed. In our rare-earth-doped materials, the charge transfer efficiency of non-radiative transitions between the rare-earth ions and the host matrix is enhanced, thereby serving as the proposed key mechanism for the improved photoelectronic performance. Our work provides a novel approach for creating large-area 2D RE materials, thereby paving the way for the industrial development of RE-based electronics and optoelectronics.

two-dimensional rare earth materials, 2D lattice anchoring strategy, field-effect transistors, photodetection, rapid photoresponse

doi: 10.1360/CSB-2025-5542